Journal of Applied Geophysics 125 (2016) 26–36

Contents lists available at ScienceDirect

Journal of Applied Geophysics

journal homepage: www.elsevier.com/locate/jappgeo

# A framework for assessing the uncertainty in wave energy delivery to targeted subsurface formations

Pranav M. Karve [a], Loukas F. Kallivokas [a,b,*], Lance Manuel [a]

[a] Department of Civil, Architectural and Environmental Engineering, The University of Texas at Austin, 301 East Dean Keeton St., Stop C1747, Austin, TX 78712, USA
[b] The Institute for Computational Engineering and Sciences (ICES), The University of Texas at Austin, 201 East 24th St., Stop C0200, Austin, TX, 78712, USA

ARTICLE INFO

*Article history:*
Received 25 March 2015
Received in revised form 13 October 2015
Accepted 1 December 2015
Available online 17 December 2015

*Keywords:*
Elastic wave energy focusing
Enhanced oil recovery
Wave propagation
Reliability analysis

ABSTRACT

Stress wave stimulation of geological formations has potential applications in petroleum engineering, hydrogeology, and environmental engineering. The stimulation can be applied using wave sources whose spatio-temporal characteristics are designed to focus the emitted wave energy into the target region. Typically, the design process involves numerical simulations of the underlying wave physics, and assumes a perfect knowledge of the material properties and the overall geometry of the geostructure. In practice, however, precise knowledge of the properties of the geological formations is elusive, and quantification of the reliability of a deterministic approach is crucial for evaluating the technical and economical feasibility of the design. In this article, we discuss a methodology that could be used to quantify the uncertainty in the wave energy delivery. We formulate the wave propagation problem for a two-dimensional, layered, isotropic, elastic solid truncated using hybrid perfectly-matched-layers (PMLs), and containing a target elastic or poroelastic inclusion. We define a wave motion metric to quantify the amount of the delivered wave energy. We, then, treat the material properties of the layers as random variables, and perform a first-order uncertainty analysis of the formation to compute the probabilities of failure to achieve threshold values of the motion metric. We illustrate the uncertainty quantification procedure using synthetic data.



## 1. Introduction

Elastic wave stimulation of subsurface formations (Fig. 1(a)) can be used as a primary or secondary recourse for enhanced oil recovery, removal of trapped contaminant particles from aquifers, subsurface colloidal transport of contaminants at waste disposal sites, etc. (Beresnev and Johnson, 1994; Kouznetsov et al., 1998; Roberts et al., 2001; Kostrov and Wooden, 2002; Vogler and Chrysikopoulos, 2002; Iassonov and Beresnev, 2003; Pride et al., 2008; Roberts and Abdel-Fattah, 2009; Beresnev and Deng, 2010; Beresnev et al., 2011; Manga et al., 2012; Lo et al., 2012; Deng and Cardenas, 2013). The utility of the stimulation depends upon, among other factors, the magnitude of the wave motion generated in the target zone. When artificial wave sources (e.g., Vibroseis) are used to apply the stimulation, equipment limitations, and geometric as well as material attenuation pose challenges in delivering sufficient vibrational energy to the target formation. Consequently, the selection of locations and frequency content of the wave sources that enables illumination of the target zone with a strong wave field is key to the success of the aforementioned engineering applications.

If the geometric description and material properties of the heterogeneous geostructure in question are known, then numerical-simulation-based techniques can be used to compute the source characteristics that focus the wave energy into the target formation. For example, if the locations of the wave sources are fixed (due to, say, practical constraints), or are assumed to be fixed, then a frequency sweep can be performed to obtain the source-time-signals maximizing the wave motion in the target. The frequency sweep uses a mathematical abstraction of the underlying wave physics (Fig. 1(b)) to compute a predefined motion metric of the target zone for a range of frequencies driving the sources. The source frequency corresponding to the maximum value of the motion metric can be used to design monochromatic source signals that deliver energy to the target, albeit not necessarily optimally or maximally. Alternatively, the problem can be cast as a search for the optimal spatio-temporal characteristics of the wave sources. This approach formally gives rise to an inverse source problem (Jeong et al., 2015; Karve et al., 2015; Karve and Kallivokas, 2015), which, upon resolution, yields optimal source time signals and locations that maximize the chosen motion metric of the target region. Time reversal (TR) is another technique that can be used to focus energy in the region of interest (Anderson et al., 2008; Ulrich et al., 2009). It consists of a two-step process. In the first step, the ground surface, or portion of the same, is populated by a

* Correspondingauthor at: Department of Civil, Architectural and Environmental Engineering, The University of Texas at Austin, 301 East Dean Keeton St., Stop C1747, Austin, TX 78712, USA.
*E-mail addresses:* pranav.karve@utexas.edu (P.M. Karve), loukas@mail.utexas.edu (L.F. Kallivokas), lmanuel@mail.utexas.edu (L. Manuel).

http://dx.doi.org/10.1016/j.jappgeo.2015.12.001
0926-9851/

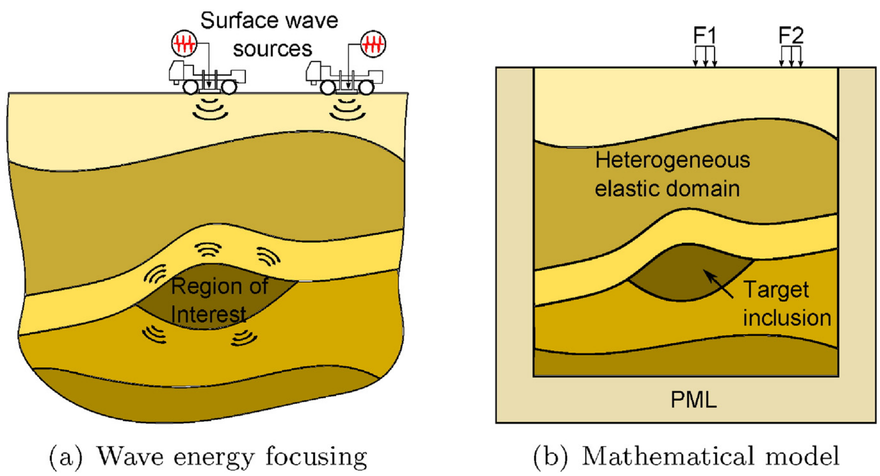


**Fig. 1.** Wave energy focusing to subterranean formations. (a) Wave energy focusing. (b) Mathematical model.

receiver array (the time reversal mirror), and a source is placed in the target region. The waves emitted by the source are recorded by the receiver array. In the second step, the signals recorded at all the receivers are time reversed, and broadcast from their respective locations. The rebroadcast waves, despite the limited mirror, could focus energy albeit imperfectly. As placing wave sources in the target may be infeasible or impractical, the first step can be performed in a numerical simulation. The signals measured at the load locations can be time reversed, and used as source excitations in the field to achieve the desired focusing. Thus, in summary, various techniques can be used to determine either an optimal, or advantageous, spatio-temporal description of the wave sources for focusing energy to a target subsurface formation.

The reliability of a methodology based on deterministic numerical modeling of the wave propagation phenomenon depends upon the accuracy of: a) the mathematical model, b) the numerical approximation, and c) the material and geometric data, which, for a layered geostructure, consists of the elastic properties of the layers, and the geometries of the interfaces between the layers. Precise knowledge of the elastic properties of the geological formations is difficult to obtain in practice. Consequently, quantification of the effects of uncertainties in the material properties on the outcome of wave propagation simulations is vital for the success of many geophysical applications.

In this article, we discuss a methodology that could be used to quantify the uncertainty in the delivery of wave energy to targeted geological formations. Our working hypotheses are: a) the mathematical model and the numerical approximation are sufficiently accurate, and b) the geometries of the interfaces between the layers of the geostructure in question are known with confidence, i.e., the uncertainty is confined to the values of the elastic properties of the layers. Our goal is to provide a probabilistic framework aiding the engineering decision making process for the wave-physics-simulation-based design procedures, in general, and the field implementation of wave energy focusing applications, in particular.

To this end, we formulate the wave propagation problem for a two-dimensional, isotropic, layered, elastic halfspace. We negotiate the semi-infinite extent of the domain of interest by truncating it with a buffer of hybrid perfectly-matched-layers (PMLs) (Kucukcoban and Kallivokas, 2013). The layered elastic domain contains a target inclusion, and tractions applied on the loaded boundary (ground surface) initiate the wave motion. We define a motion metric for the target inclusion to measure the amount of the wave energy delivered to the target. We assume that the geometric description of the geostructure is known, and that the mean values of the material properties of the layers, as well as the associated (marginal) probability distribution functions (PDFs) have been computed, using, for example, the procedure described by Gouveia and Scales (Gouveia and Scales, 1998). The uncertainty analysis is used to compare the performance of candidate spatio-temporal characteristics of the wave sources (optimal, or otherwise). Note that the candidate source specifications can be computed using the deterministic wave simulations mentioned earlier. The quantification of uncertainty in the value of the motion metric is carried out in two steps. In the first step, we perform a first-order sensitivity analysis of the elastodynamic system to calibrate the dependence of the motion metric on each of the Lamé parameters. This (deterministic) sensitivity analysis computes the derivative of the motion metric with respect to a material parameter at a given (assumed) set of the properties. In the next step, we treat the Lamé parameters as random variables with known probability distribution functions (PDFs). We, then, use the Rackwitz-Fiessler algorithm (Rackwitz and Fiessler, 1978) to perform a first-order uncertainty analysis of the elastodynamic system. This analysis allows estimation of the probabilities of failure to attain any specified threshold values of the motion metric.

In the following sections, we discuss in detail: a) the mathematical and computational model for the associated wave physics, b) the first-order sensitivity analysis, and c) the first-order uncertainty analysis using the Rackwitz-Fiessler algorithm, respectively. As an example, we present the results of uncertainty quantification for a synthetic geological formation model, and optimal loads reported in (Karve et al., 2015). Next, we illustrate how the proposed methodology can be easily extended to quantify the uncertainty in the wave delivery to a poroelastic target inclusion embedded in an elastic geostructure. Lastly, we outline a candidate design procedure for the field implementation of the wave-based enhanced oil recovery method (or other similar applications of wave energy delivery to targeted geological formations).

## 2. The mathematical and computational model

The governing equations for a two-dimensional, heterogeneous, isotropic, elastic solid ($\Omega_{\text{reg}}$, Fig. 2), truncated by PMLs ($\Omega_{\text{PML}}$, Fig. 2), and enclosing a target inclusion ($\Omega_{\text{a}}$, Fig. 2), for time $t \in (0, T] = J$, are given as:

$$\mathbf{div}\left[\mu_{\text{a}}\left(\nabla\mathbf{u}_{\text{a}} + \nabla\mathbf{u}_{\text{a}}^{T}\right) + \{\lambda_{\text{a}}\text{div}\,\mathbf{u}_{\text{a}}\}\mathbf{I}\right] - \rho_{\text{a}}\ddot{\mathbf{u}}_{\text{a}} = 0, \mathbf{x} \in \Omega_{\text{a}}, \tag{1}$$

and,

$$\mathbf{div}\left[\mu_{\text{b}}\left(\nabla\mathbf{u}_{\text{b}} + \nabla\mathbf{u}_{\text{b}}^{T}\right) + \{\lambda_{\text{b}}\text{div}\,\mathbf{u}_{\text{b}}\}\mathbf{I}\right] - \rho_{\text{b}}\ddot{\mathbf{u}}_{\text{b}} = 0, \mathbf{x} \in \Omega_{\text{reg}}, \tag{2a}$$

$$\mathbf{div}\left(\dot{\mathbf{S}}^{T}\tilde{\Lambda}_{e} + \mathbf{S}^{T}\tilde{\Lambda}_{p}\right) - \rho_{\text{b}}\left(\mathrm{a}\ddot{\mathbf{u}}_{\text{b}} + \mathrm{b}\dot{\mathbf{u}}_{\text{b}} + \mathrm{c}\mathbf{u}_{\text{b}}\right) = 0, \mathbf{x} \in \Omega_{\text{PML}}, \tag{2b}$$

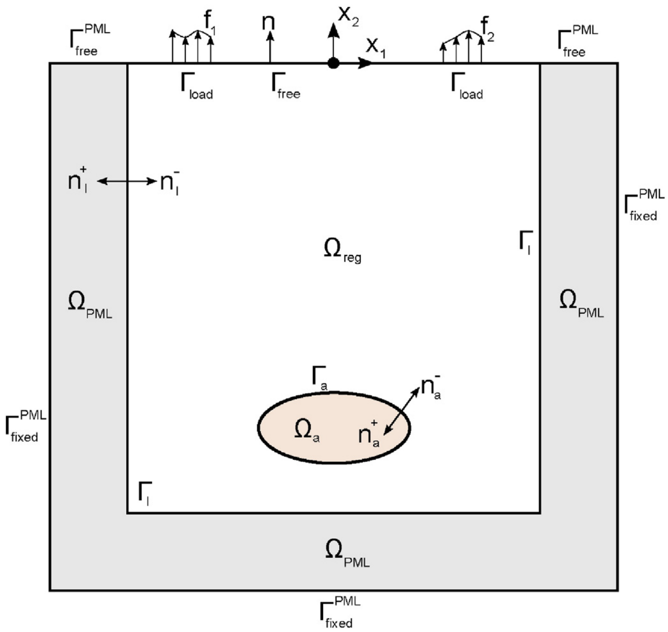


**Fig. 2.** Problem definition.

$$\mathcal{D}:\left(\mathrm{a}\ddot{\mathbf{S}}+\mathrm{b}\dot{\mathbf{S}}+\mathrm{c}\mathbf{S}\right)-\frac{1}{2}\left[\nabla\mathbf{u}_{\mathrm{b}}\tilde{\Lambda}_p+\tilde{\Lambda}_p(\nabla\mathbf{u}_{\mathrm{b}})^T+\nabla\dot{\mathbf{u}}_{\mathrm{b}}\tilde{\Lambda}_e+\tilde{\Lambda}_e(\nabla\dot{\mathbf{u}}_{\mathrm{b}})^T\right]=0,\mathbf{x}\in\Omega_{\mathrm{PML}}, \tag{2c}$$

where an overdot, $(\dot{\cdot})$, denotes a derivative with respect to time, a colon, $(:)$, represents tensor inner product, and spatial as well as temporal dependencies are suppressed for brevity. Eqs. (1), (2a), (2b), (2c) are the elastodynamics equations for a semi-infinite medium, augmented by PMLs (Kucukcoban and Kallivokas, 2013). Specifically, Eqs. (1), (2a), and (2b) are equilibrium equations, whereas Eq. (2c) is the combined constitutive law and kinematic condition equation. $\mathbf{u}_{\mathrm{a}}(\mathbf{x},t)$ represents the displacement field in the target inclusion $\Omega_{\mathrm{a}}$, whereas $\mathbf{u}_{\mathrm{b}}(\mathbf{x},t)$ denotes the displacement in the rest of the domain $(\Omega_{\mathrm{reg}}\cup\Omega_{\mathrm{PML}})$. $\mathbf{S}(\mathbf{x},t)$ is the stress *history* tensor in $\Omega_{\mathrm{PML}}$, given by,

$$\mathbf{S}(\mathbf{x},t)=\begin{bmatrix}\mathbf{S}_{11}(\mathbf{x},t) & \mathbf{S}_{11}(\mathbf{x},t)\\ \mathbf{S}_{21}(\mathbf{x},t) & \mathbf{S}_{22}(\mathbf{x},t)\end{bmatrix}=\int_0^t\sigma(\mathbf{x},\tau)d\tau, \tag{3}$$

where $\sigma$ is the Cauchy stress tensor. $\tilde{\Lambda}_e$ and $\tilde{\Lambda}_p$ are components of the stretching tensor, and a,b,c are coefficients defining complex co-ordinate stretching in the PML region. Their detailed definitions are beyond the scope of this article and can be found in (Kucukcoban and Kallivokas, 2013). $(\lambda_{\mathrm{a}},\mu_{\mathrm{a}},\rho_{\mathrm{a}})$ and $(\lambda_{\mathrm{b}},\mu_{\mathrm{b}},\rho_{\mathrm{b}})$ are the Lamé parameters and mass density for the inclusion $\Omega_{\mathrm{a}}$ and $\Omega_{\mathrm{reg}}\cup\Omega_{PML}$, respectively. $\mathcal{D}$ is the compliance tensor, so that the constitutive law takes the form $\mathcal{D}:\dot{\mathbf{S}}=\frac{1}{2}(\nabla\mathbf{u}_{\mathrm{b}}+\nabla\mathbf{u}_{\mathrm{b}}^T)$. For $t\in J$, the governing equations are subjected to the following boundary conditions:

$$\mathbf{u}_{\mathrm{b}}=0,\qquad \mathbf{x}\in\Gamma_{\mathrm{fixed}}^{\mathrm{PML}}, \tag{4a}$$

$$\sigma_b^T\mathbf{n}=\mathbf{f}(\mathbf{x},t),\qquad \mathbf{x}\in\Gamma_{\mathrm{load}}, \tag{4b}$$

$$\sigma_b^T\mathbf{n}=0,\qquad \mathbf{x}\in\Gamma_{\mathrm{free}}, \tag{4c}$$

$$\left(\dot{\mathbf{S}}^T\tilde{\Lambda}_e+\mathbf{S}^T\tilde{\Lambda}_p\right)\mathbf{n}=0,\qquad \mathbf{x}\in\Gamma_{\mathrm{free}}^{\mathrm{PML}}; \tag{4d}$$

interface conditions:

$$\mathbf{u}_{\mathrm{b}}^+=\mathbf{u}_{\mathrm{b}}^-,\qquad \mathbf{x}\in\Gamma_{\mathrm{I}}, \tag{5a}$$

$$\sigma_{\mathrm{b}}^T\mathbf{n}_{\mathrm{I}}^+=-\left(\dot{\mathbf{S}}^T\tilde{\Lambda}_e+\mathbf{S}^T\tilde{\Lambda}_p\right)\mathbf{n}_{\mathrm{I}}^-,\qquad \mathbf{x}\in\Gamma_{\mathrm{I}}, \tag{5b}$$

$$\mathbf{u}_{\mathrm{a}}=\mathbf{u}_{\mathrm{b}},\qquad \mathbf{x}\in\Gamma_{\mathrm{a}}, \tag{5c}$$

$$\sigma_{\mathrm{a}}^T\mathbf{n}_{\mathrm{a}}^-=-\sigma_{\mathrm{b}}^T\mathbf{n}_{\mathrm{a}}^+,\qquad \mathbf{x}\in\Gamma_{\mathrm{a}}; \tag{5d}$$

where,

$$\sigma_{\mathrm{a}}=\mu_{\mathrm{a}}(\nabla\mathbf{u}_{\mathrm{a}}+\nabla\mathbf{u}_{\mathrm{a}}^T)+\lambda_{\mathrm{a}}(\mathrm{div}\,\mathbf{u}_{\mathrm{a}})\mathbf{I}, \tag{5e}$$

$$\sigma_{\mathrm{b}}=\mu_{\mathrm{b}}(\nabla\mathbf{u}_{\mathrm{b}}+\nabla\mathbf{u}_{\mathrm{b}}^T)+\lambda_{\mathrm{b}}(\mathrm{div}\,\mathbf{u}_{\mathrm{b}})\mathbf{I}; \tag{5f}$$

and initial conditions:

$$\mathbf{u}_{\mathrm{a}}(\mathbf{x},0)=0,\quad \dot{\mathbf{u}}_{\mathrm{a}}(\mathbf{x},0)=0,\qquad \mathbf{x}\in\Omega_{\mathrm{a}}, \tag{6a}$$

$$\mathbf{u}_{\mathrm{b}}(\mathbf{x},0)=0,\quad \dot{\mathbf{u}}_{\mathrm{b}}(\mathbf{x},0)=0,\qquad \mathbf{x}\in\Omega_{\mathrm{reg}}\cup\Omega_{\mathrm{PML}}, \tag{6b}$$

$$\mathbf{S}(\mathbf{x},0)=0,\quad \dot{\mathbf{S}}(\mathbf{x},0)=0,\qquad \mathbf{x}\in\Omega_{\mathrm{PML}}. \tag{6c}$$

The tractions $\mathbf{f}(\mathbf{x},t)$ applied on $\Gamma_{\mathrm{load}}$ consist of contributions $\mathbf{f}_i(\mathbf{x},t)$ from $n_s$ sources. The $i$-th source consists of a spatial $\theta_i(\mathbf{x})$ and a temporal $f_i(t)$ component. $\theta_i$ is further decomposed into the $x_1$-directional component $\theta_{i1}(\mathbf{x})$ and the $x_2$-directional component $\theta_{i2}(\mathbf{x})$. Thus,

$$\mathbf{f}(\mathrm{x},t)=\sum_{i=1}^{n_s}\mathbf{f}_i(\mathrm{x},t)=\sum_{i=1}^{n_s}\begin{bmatrix}\theta_{i1}(\mathrm{x})\\ \theta_{i2}(\mathrm{x})\end{bmatrix}f_i(t). \tag{7}$$

In this work, we use horizontally polarized loads that vary like a Gaussian function on the loaded boundary $(x_2=0)$, i.e., $\theta_{i1}(\mathbf{x})=0$, and,

$$\theta_{i2}(\mathbf{x})=\exp\left[-\frac{(x_1-\eta_i)^2}{b_i}\right],\quad i=1,2,\ldots,n_s. \tag{8}$$

Notice that the parameter $\eta_i$ controls the location of the center line of the load, and that $b_i$ defines the width of the load. We employ the finite element method to resolve the initial boundary value problem defined by Eqs. (1)–(6c). To this end, we cast the governing Eqs. (1), (2a), (2b), (2c) in their weak form. We, then, introduce spatial discretization via continuous Lagrange shape functions to arrive at the following semi-discrete equation:

$$\mathbf{M}\ddot{\mathbf{y}}(t)+\mathbf{C}\dot{\mathbf{y}}(t)+\mathbf{K}\mathbf{y}(t)=\mathbf{F}(t), \tag{9}$$

where,

$$\mathbf{y}=\left[\tilde{\mathbf{u}}_{\mathrm{a}_1}\,\tilde{\mathbf{u}}_{\mathrm{a}_2}\left|\tilde{\mathbf{u}}_{\mathrm{b}_1}^{\mathrm{reg}}\,\tilde{\mathbf{u}}_{\mathrm{b}_2}^{\mathrm{reg}}\right|\tilde{\mathbf{u}}_{\mathrm{b}_1}^{\mathrm{PML}}\,\tilde{\mathbf{u}}_{\mathrm{b}_2}^{\mathrm{PML}}\,\tilde{\mathbf{S}}_{11}\,\tilde{\mathbf{S}}_{22}\,\tilde{\mathbf{S}}_{12}\right]^T, \tag{10}$$

$$\mathbf{F}=\left[00\mathbf{F}^1\,\mathbf{F}^2 00000\right]^T. \tag{11}$$

The quantities with a tilde over the quantity symbol $(\tilde{\ })$ denote vectors of nodal values of the subtended quantity. We note that **M,C**, and **K** are the global mass, damping, and stiffness matrices, respectively, **y** is the vector of unknown displacements (everywhere) and stress histories (PML only), and **F** is the force vector. Further details of the global and element matrices can be found in (Kucukcoban and Kallivokas, 2013; Karve et al., 2015).

The temporal dimension is now discretized using a timestep $\Delta t$. We define the vector $\mathbf{y}_i=\mathbf{y}$, at time $t=i\Delta t$. The equation of motion of the spatio-temporally discretized system at time $t=(i+1)\,\Delta t$, can be written as:

$$\mathbf{M}\ddot{\mathbf{y}}_{i+1}+\mathbf{C}\dot{\mathbf{y}}_{i+1}+\mathbf{K}\mathbf{y}_{i+1}=\mathbf{F}_{i+1}. \tag{12}$$

**Table 1**
Material properties for the layers and the inclusion shown in the geological formation model (Fig. 5(a)).

| Layer | λ(MPa) | μ(MPa) |
|---|---|---|
| L1 | 416.67 | 625.00 |
| L2 | 694.44 | 1041.67 |
| L3 | 972.22 | 1458.33 |
| L4 | 1250.00 | 1875.00 |
| T | 277.78 | 416.67 |

We employ Newmark's time integration scheme to integrate Eq. (12) in time. The time histories of the state variables $\ddot{\mathbf{y}}, \dot{\mathbf{y}}, \mathbf{y}$ can now be computed given the force vector $\mathbf{F}$. The time histories will be used to calculate the motion metric measuring the intensity of energy focusing. Next, we define the motion metric, and select candidate source specifications for a synthetic geo-formation.

## 3. Wave energy focusing

Given the geometry and the material properties of the geostructure in question, the spatio-temporally optimal wave sources that maximize the wave motion in a target formation can be obtained using the computational model (Eq. (12)), and one of the aforementioned methods (frequency sweep, TR, or inverse source method). Once the optimal load characteristics are calculated, one can perform the sensitivity and reliability analyses to quantify the effects of uncertainty in the input. Here, we demonstrate this process using a synthetic geological formation model (Fig. 5a). The formation model contains four layers (L1-L4) and a target inclusion (T). In a deterministic approach, we assume that the material properties of the layers ($\lambda_{bi}$,$\mu_{bi}$) and the inclusion ($\lambda_a$,$\mu_a$), as well as the interface geometries are known with confidence. As an example, consider the values of the Lamé parameters given in Table 1. The mass density for all layers is 2200 kg/$m^3$.

To measure the intensity of energy focusing, we define the motion metric in terms of the time-averaged kinetic energy. If $\mathbf{u}(t)$ denotes the displacement at a computational node at time $t$, then the time-averaged kinetic energy ($KE_{TA}$) at that node is defined as:

$$KE_{TA} = \int_0^T \frac{1}{2}\rho[\dot{\mathbf{u}}(t)\cdot\dot{\mathbf{u}}(t)]dt/T, \tag{13}$$

where $\rho$ is the mass density. Time-averaged kinetic energy, further integrated over the target inclusion, is defined as $KE_{inc}$. Thus,

$$\begin{aligned} KE_{inc} &= \int_{\Omega_a}\int_0^T \frac{1}{2}\rho_a[\dot{\mathbf{u}}_a(t)\cdot\dot{\mathbf{u}}_a(t)]\mathrm{d}t\,d\Omega/T \\ &= \int_0^T \frac{1}{2}\dot{\mathrm{u}}_a(t)^T\mathbf{M}_{inc}\dot{\mathbf{u}}_a(t)\mathrm{d}t/T, \end{aligned} \tag{14}$$

where $\dot{\mathrm{u}}_a(t)$ is the velocity vector corresponding to the computational nodes in the inclusion, and $\mathbf{M}_{inc}$ is the mass matrix of the inclusion. The units of $KE_{TA}$ are J/m$^3$, and those of $KE_{inc}$ are J/m. We use plots of $KE_{TA}$ and values of $KE_{inc}$ to compare the degree of energy focusing achieved by candidate source specifications. The effectiveness of the stress wave stimulation can be assessed by comparing the metric ($KE_{inc}$) with a threshold value ($\mathcal{KE}_{th}$), where the threshold is selected based on the engineering application of interest.

In (Karve et al., 2015), an inverse source approach was followed for the geological formation model (Fig. 5(a)) endowed with the properties given in Table 1, and the source characteristics that maximize the wave energy delivery to the target inclusion were computed. In one of the numerical experiments (experiment 2), the inversion process was carried out for three horizontally polarized loads applied on the ground surface. Here, we use two sets of optimal (converged) load characteristics reported in that experiment, specifically: a) the optimal time signals obtained without changing the load locations (load case A), and b) the optimal time signals and locations obtained by a simultaneous spatio-temporal optimization process (load case B). Figs. 3 and 4 show the optimal time signals for the two cases. Fig. 5(b) and (c) show the plots of time averaged kinetic energy. The focusing of kinetic energy in the target inclusion is clearly seen in these figures. Table 2 summarizes the optimal source characteristics and the resulting ($KE_{inc}$) values. Further details of the inversion methodology can be found in (Karve et al., 2015). In the following sections, we outline the sensitivity and uncertainty analyses, respectively, and illustrate their use for the load cases A and B.

## 4. Sensitivity analysis

The sensitivity analysis quantifies the dependence of the motion metric on the value of a particular system parameter (Lamé parameter) by calculating the relevant derivative. Here, we use the procedure discussed in (Tsikas, 1997; Van Keulen et al., 2005) to perform sensitivity analysis of the second-order elastodynamic system (Eq. (9)). We define a vector ($\mathbf{q}$) of Lamé parameters for the layers and the inclusion (i.e., the system parameters):

$$\mathbf{q} = [q_1\; q_2 \ldots q_N]^T = \left[\lambda_{b_1}\;\lambda_{b_2}\ldots\lambda_a\;\mu_{b_1}\;\mu_{b_2}\ldots\mu_a\right]^T. \tag{15}$$

Now, the semi-discrete equilibrium Eq. (9) can be rewritten as:

$$\mathbf{M}(\mathbf{q})\ddot{\mathbf{y}}(\mathbf{q}) + \mathbf{C}(\mathbf{q})\dot{\mathbf{y}}(\mathbf{q}) + \mathbf{K}(\mathbf{q})\mathbf{y}(\mathbf{q}) = \mathbf{F}, \tag{16}$$

where we have explicitly shown the dependence of the system matrices and state variables on $\mathbf{q}$. The goal of the sensitivity analysis is to compute $\mathbf{z}^i = \frac{\partial \mathbf{y}}{\partial q_i}$ and its time derivatives for $i = 1,2,\ldots,N$. To this end, we

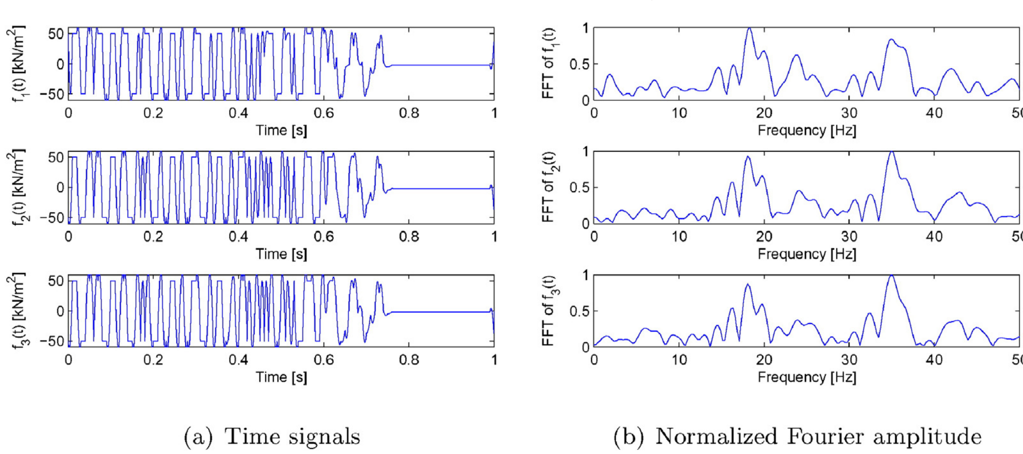


**Fig. 3.** Optimal time signals (obtained without changing load locations) and associated frequency content. (a) Time signals. (b) Normalized Fourier amplitude.

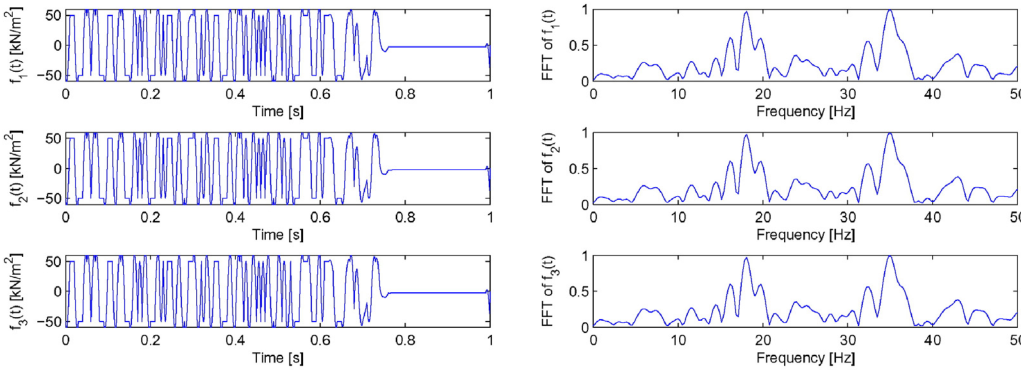


(a) Time signals (b) Normalized Fourier amplitude

**Fig. 4.** Optimal time signals and associated frequency content after simultaneous time signal-location optimization. (a) Time signals. (b) Normalized Fourier amplitude.

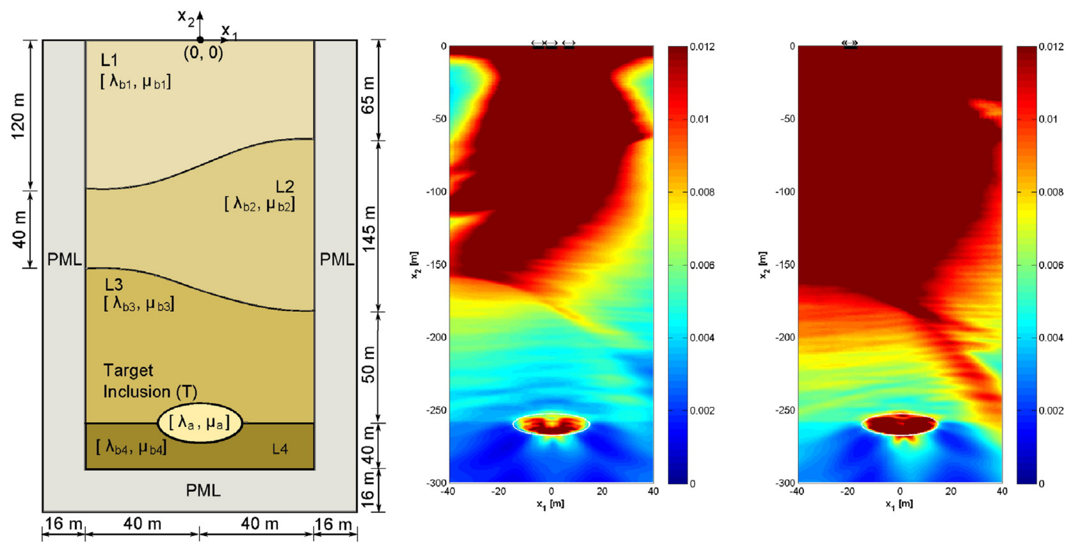


(a) Geological formation model (b) $KE_{TA}$ after time signal optimization (load case A) (c) $KE_{TA}$ after time signal and load-location optimization (load case B)

**Fig. 5.** Geological formation model and plots of time-averaged kinetic energy ($KE_{TA}$). (a) Geological formation model. (b) $KE_{TA}$ after time signal optimization (load case A). (c) $KE_{TA}$ after time signal and load-location optimization (load case B).

perturb the $i$-th parameter ($q_i$) using an increment $\epsilon \to 0$. We, then, write the equilibrium equation for the perturbed system. After some algebraic simplifications, and neglecting second ordered terms in $\epsilon$, we arrive at the following equation for the sensitivity variable $\mathbf{z}^i$:

$$\mathbf{M}(\mathbf{q})\ddot{\mathbf{z}}^i + \mathbf{C}(\mathbf{q})\dot{\mathbf{z}}^i + \mathbf{K}(\mathbf{q})\mathbf{z}^i = -\frac{\partial \mathbf{M}(\mathbf{q})}{\partial q_i}\ddot{\mathbf{y}}(\mathbf{q}) - \frac{\partial \mathbf{C}(\mathbf{q})}{\partial q_i}\dot{\mathbf{y}}(\mathbf{q}) - \frac{\partial \mathbf{K}(\mathbf{q})}{\partial q_i}\mathbf{y}(\mathbf{q}). \quad (17)$$

The right hand side of Eq. (17) requires assembly of the derivatives of the system matrices, which is performed using the derivatives of the element matrices given in Appendix A. We discretize the time line using timestep $\Delta t$. We define the vector $\mathbf{z}_j^i = \mathbf{z}^i$, at time $t = j\Delta t$. The equation of motion for the sensitivity variables, at time $t = j\Delta t$, can be written as:

$$\mathbf{M}(\mathbf{q})\ddot{\mathbf{z}}_j^i + \mathbf{C}(\mathbf{q})\dot{\mathbf{z}}_j^i + \mathbf{K}(\mathbf{q})\mathbf{z}_j^i = -\frac{\partial \mathbf{M}(\mathbf{q})}{\partial q_i}\ddot{\mathbf{y}}_j(\mathbf{q}) - \frac{\partial \mathbf{C}(\mathbf{q})}{\partial q_i}\dot{\mathbf{y}}_j(\mathbf{q}) - \frac{\partial \mathbf{K}(\mathbf{q})}{\partial q_i}\mathbf{y}_j(\mathbf{q}). \quad (18)$$

Thus, if the time histories of the state variables $(\mathbf{y}(\mathbf{q}), \dot{\mathbf{y}}(\mathbf{q}), \ddot{\mathbf{y}}(\mathbf{q}))$, and the derivatives of system matrices with respect to the material

**Table 2**
Optimal source characteristics for the geological formation model computed using the inverse source approach.

| Load case | Time signals | Location parameters (m) | $KE_{TA}$ | $KE_{inc}$ (J/m) |
|---|---|---|---|---|
| A | Fig. 3 | $\eta_1 = -7.00, \eta_2 = -5.00, \eta_3 = 0.00$ | Fig. 5(b) | 3.22 |
| B | Fig. 4 | $\eta_1 = -19.00, \eta_2 = -19.16, \eta_3 = -20.04$ | Fig. 5(c) | 4.75 |

**Table 3**
Results of sensitivity analysis (load case A).

| $q_i$ | $\frac{\partial KE_{inc}}{\partial q_i}$ (nJ/mPa) | $q_i$ | $\frac{\partial KE_{inc}}{\partial q_i}$ (nJ/mPa) |
|---|---|---|---|
| $\lambda_{b_1}$ | 0.397 | $\mu_{b_1}$ | 3.215 |
| $\lambda_{b_2}$ | 0.114 | $\mu_{b_2}$ | −1.273 |
| $\lambda_{b_3}$ | −0.020 | $\mu_{b_3}$ | −1.374 |
| $\lambda_{b_4}$ | 0.019 | $\mu_{b_4}$ | 0.468 |
| $\lambda_a$ | −0.039 | $\mu_a$ | −6.705 |

parameter of interest ($q_i$) are known, then the time histories of the sensitivity variables ($\mathbf{z}^i, \dot{\mathbf{z}}^i, \ddot{\mathbf{z}}^i$) can be computed by integrating Eq. (18), using, for example, the Newmark's method. Once the time history of the velocity-like sensitivity variable ($\dot{\mathbf{z}}^i$) is computed, the derivative of the motion metric ($\mathrm{KE_{inc}}(\mathbf{q})$), with respect to a material parameter $q_i$ can be evaluated as:

$$\frac{\partial \mathrm{KE_{inc}}(q)}{\partial q_i} = \int_0^T \dot{z}^i_{\mathrm{u_a}}(t)^T \mathrm{M_{inc}} \dot{\mathrm{u}}(t) \mathrm{d}t/T, \tag{19}$$

where $\dot{\mathbf{z}}^i_{\mathbf{u}_a}$ contains the nodal values of the velocity-like sensitivity variable corresponding to the degrees of freedom in the target inclusion.

As an illustration, we perform the sensitivity analysis for the geological formation model (Fig. 4) endowed with material properties given in Table 1. The results of sensitivity analysis for load cases A and B are summarized in Tables 3 and 4, respectively. It can be seen that the motion metric is most sensitive to the value of the second Lamé parameter (shear modulus) of the target inclusion. Out of the surrounding layers, the metric is more sensitive to the properties of the first layer for load case A, and that of the second layer for load case B. In general, the metric is less sensitive to the variation in λ values than it is to the variation in $\mu$ values.

The deterministic sensitivity analysis quantifies the effect of variation in the input data in a very limited sense. The derivatives computed in this analysis are valid only at the material state at which they are computed. The system may not exhibit similar behavior at other values of material properties. Furthermore, the sensitivity analysis provides little information about the ability of the wave sources to create strong wave motion in the target zone. To quantify the effect of uncertainty in a comprehensive manner, we discuss a probabilistic analysis next.

## 5. Uncertainty analysis

To assess the uncertainty in the wave energy delivery, we investigate probabilistically the motion metric by treating the material properties as random variables. For a layered geo-formation, if the geometry of the interfaces between the layers is (assumed to be) accurately known, and the loading is specified, then $\mathrm{KE_{inc}}$ depends on the values of material properties of the layers. Thus, the motion metric of the target inclusion is a function of $N$ random variables ($\mathbf{q}$). The uncertainty in wave energy delivery can be estimated by evaluating the probability of failure to attain a predefined threshold value ($\mathcal{KE}_{\mathrm{th}}$) of the metric,

**Table 4**
Results of sensitivity analysis (load case B).

| $q_i$ | $\frac{\partial KE_{inc}}{\partial q_i}$ (nJ/mPa) | $q_i$ | $\frac{\partial KE_{inc}}{\partial q_i}$ (nJ/mPa) |
|---|---|---|---|
| $\lambda_{b_1}$ | 0.379 | $\mu_{b_1}$ | −0.501 |
| $\lambda_{b_2}$ | 0.485 | $\mu_{b_2}$ | 2.735 |
| $\lambda_{b_3}$ | 0.036 | $\mu_{b_3}$ | −2.596 |
| $\lambda_{b_4}$ | 0.044 | $\mu_{b_4}$ | 0.819 |
| $\lambda_a$ | −0.359 | $\mu_a$ | −9.793 |

i.e., $P[\mathrm{KE}_{inc}(\mathbf{q}) < \mathcal{KE}_{\mathrm{th}}]$. If the joint probability distribution function (PDF) for the random system variables, $f_{\mathbf{Q}}(q_1, q_2, \ldots, q_N)$, is known, then the required probability can be evaluated as,

$$P[\mathrm{KE_{inc}}(\mathbf{q}) < \mathcal{KE}_{\mathrm{th}}] = \int \cdots \int_{\mathrm{KE_{inc}}(\mathbf{q}) < \mathcal{KE}_{\mathrm{th}}} f_{\mathbf{Q}}(q_1, q_2, \ldots, q_N) dq_1 dq_2 \ldots dq_N. \tag{20}$$

The integral on the right hand side of Eq. (20) is evaluated over the region where $\mathrm{KE_{inc}}(\mathbf{q}) < \mathcal{KE}_{\mathrm{th}}$. Typically, only the marginal PDFs ($f_{Q_i}(q_i)$) for the individual random variables ($q_i$) are known, and the joint PDF is difficult to obtain. Hence, approximate methods are required to evaluate $P[\mathrm{KE_{inc}}(\mathbf{q}) \cdot < \mathcal{KE}_{\mathrm{th}}]$. In this work, we favor a first-order approach for computing the integral in Eq. (20). The first-order analysis requires computation of the first derivatives of the motion metric with respect to the random system variables ($q_i$), or, $\frac{\partial KE_{inc}(\mathbf{q})}{\partial q_i}$ for $i = 1, 2, \ldots, N$. Note that we calculated the required derivatives in the sensitivity analysis (Eq. (19)). We remark that a more accurate, second-order approach requires computation of the Hessian of $\mathrm{KE_{inc}}(\mathbf{q})$ in the $N$-dimensional space, which is prohibitively expensive for large elastodynamic systems.

We employ the Rackwitz-Fiessler algorithm (Appendix C, (Rackwitz and Fiessler, 1978))to perform the first-order uncertainty analysis. In this algorithm, the original (correlated or uncorrelated) random variables ($\mathbf{q}$) are mapped to uncorrelated, standard normal random variables ($\mathbf{U}$) using a linear transformation. The joint PDF ($f_{\mathrm{U}}(U_1, \cdots, U_N)$) can now be easily computed as the product of $N$ standard normal PDFs. The surface $\mathrm{KE_{inc}}(\mathbf{q}) = \mathcal{KE}_{\mathrm{th}}$ is approximated as a first-order surface (an $N$-dimensional hyperplane) to enable an efficient but approximate computation of the integral in Eq. (20).

We illustrate the probabilistic analysis procedure using the geological formation model shown in Fig. 5(a). The mean value and standard deviation vectors corresponding to the vector of Lamé parameters ($\mathbf{q}$) are denoted by $\overline{\mathbf{q}}$ and $\mathbf{D}$, respectively. We assume that the Lamé parameter values given in Table 1 are the mean values ($\overline{\mathbf{q}}$), the wave motion is actuated by the (optimal) loads given in Table 2 (load cases A and B), and the material properties are uncorrelated, normally distributed random variables. We remark that the methodology can easily accommodate other types of probability distributions as well as correlated random variables.

Initially, we use the same coefficient of variation for the entire geostructure, i.e., $D_i = C_v \overline{q}_i$, for $i = 1,2,\ldots,N$ for a fixed value of $C_v$. This assumption will be relaxed later. We compute the failure probabilities for a range of thresholds of the motion metric, given the values of $\overline{\mathbf{q}}$ and $C_v$. The results for load cases A and B are plotted in Figs. 6 and 7,

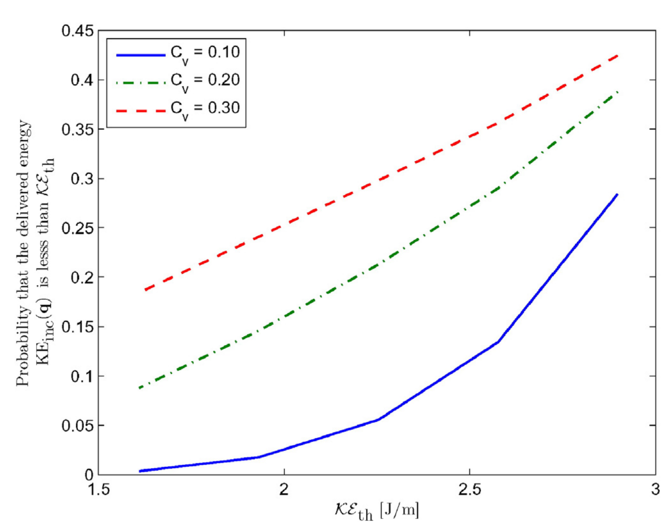


**Fig. 6.** Results of uncertainty analyses using the same $C_v$ value for all layers (load case A).

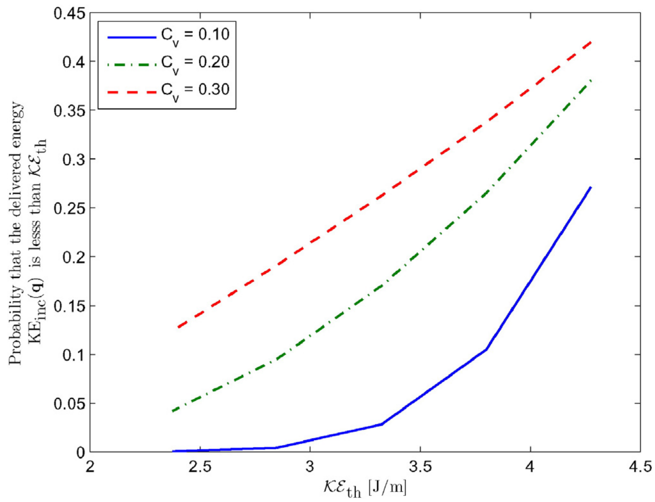


**Fig. 7.** Results of uncertainty analyses using the same $C_v$ value for all layers (load case B).

respectively. It can be seen that for a given $\mathcal{KE}_{\text{th}}$ value, $P[\text{KE}_{\text{inc}}(\mathbf{q}) < \mathcal{KE}_{\text{th}}]$ decreases as $C_v$ decreases. It is also evident that $P[\text{KE}_{\text{inc}}(\mathbf{q}) < \mathcal{KE}_{\text{th}}]$ reduces with the value of $\mathcal{KE}_{\text{th}}$ for a given $C_v$.

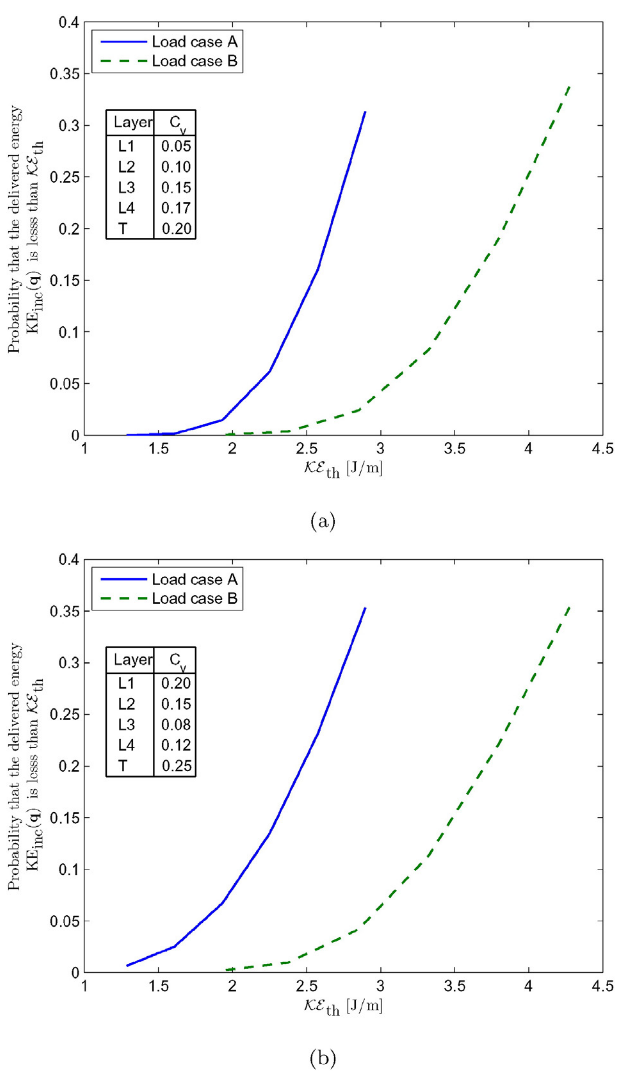


**Fig. 8.** Results of uncertainty analyses using different $C_v$ values for different layers.

Alternatively, the uncertainty in our knowledge of the material properties of the layered geostructure can be captured by assigning different $C_v$ values to different layers (Gouveia and Scales, 1998). Fig. 8 shows the results of uncertainty analyses for such cases (the assumed $C_v$ values for the layers are shown in a table within the figure). It can be seen in Fig. 8 that the spatio-temporally optimized loads (load case B) have a higher probability of achieving a given value of the motion metric than the loads whose locations were kept fixed while optimizing the time-signals (load case A). These analyses can be used to compare the effectiveness of candidate loads in delivering wave energy to the target formation, when the material properties of the geostructure are not known with confidence.

## 6. Wave energy delivery to a poroelastic target inclusion

In the preceding sections, we discussed how the uncertainty in wave energy delivery to a subsurface elastic formation can be quantified using sensitivity and uncertainty analyses. The laboratory and analytical investigations into the release of trapped particles from the pores of geological formations (Beresnev and Johnson, 1994; Kouznetsov et al., 1998; Roberts et al., 2001; Kostrov and Wooden, 2002; Vogler and Chrysikopoulos, 2002; Iassonov and Beresnev, 2003; Pride et al., 2008; Roberts and Abdel-Fattah, 2009; Beresnev and Deng, 2010; Beresnev et al., 2000; Manga et al., 2012; Lo et al., 2012; Deng and Cardenas, 2013) suggest that an estimate of the fluid motion in the target formation can lead to a better assessment of the particle mobilization phenomenon. In order to estimate the fluid motion generated due to the applied stress wave stimulation, in this section, we consider the case of a poroelastic target inclusion ($\Omega_a$, Fig. 2) embedded in a heterogeneous, elastic halfspace. We use Biot's equations of poroelastodynamics (Biot, 1956) to model the wave propagation in the poroelastic target. Thus, the response in the poroelastic target inclusion ($\Omega_a$) is described by a solid and a fluid displacement field, $\mathbf{u}_{\text{a}}$, and $\mathbf{u}_{\text{f}}$, respectively. We favor the u-w form of the Biot's equations (Biot, 1956; Schanz, 2009) to model the wave propagation in the poroelastic target. The u-w form uses the seepage displacement $\mathbf{w} = \phi(\mathbf{u}_{\text{f}} - \mathbf{u}_{\text{a}})$, where $\phi$ is the porosity, to describe the fluid displacement field in the poroelastic target $\Omega_{\text{a}}$ (Schanz, 2009). The governing equations in $\Omega_{\text{a}}$, for time $t \in \text{J} = (0, T]$, are given by:

$$\text{div}\left[\mu_{\text{a}}\left(\nabla\mathbf{u}_a + \nabla\mathbf{u}_a^T\right) + \left\{\left(\lambda_{\text{a}} + \alpha^2 M\right)\text{div}\,\mathbf{u}_a + \alpha M\,\text{div}\,\mathbf{w}\right\}\mathbf{I}\right] - \rho_{\text{a}}\ddot{\mathbf{u}}_a - \rho_f\ddot{\mathbf{w}} = 0, \mathbf{x} \in \Omega_{\text{a}}, \tag{21a}$$

$$\text{div}[\{\alpha M\,\text{div}\,\mathbf{u}_{\text{a}} + M\,\text{div}\,\mathbf{w}\}\mathbf{I}] - \rho_f\ddot{\mathbf{u}}_{\text{a}} - \rho_f\frac{1 + C_1}{\phi}\ddot{\mathbf{w}} - \frac{1}{\kappa}\dot{\mathbf{w}} = 0, \mathbf{x} \in \Omega_a, \tag{21b}$$

where an overdot, $(\dot{\cdot})$, denotes a derivative of the subtended entity with respect to time, and the temporal and spatial dependencies have been suppressed for brevity. The parameters $\lambda_{\text{a}}$ and $M$ are defined as:

$$\lambda_{\text{a}} = \lambda_s - \alpha\left(\lambda_s + \frac{2}{3}\mu_s\right), \quad M = \frac{1}{\dfrac{\alpha - \phi}{\lambda_s + \frac{2}{3}\mu_s} + \dfrac{\phi}{\lambda_f}}, \tag{22}$$

where $\lambda_s$ and $\lambda_f$ denote the first Lamé parameter for the solid grains and the interstitial fluid, respectively. $\mu_{\text{a}} = \mu_s$, is the second Lamé parameter (shear modulus) of the solid grains in the poroelastic target inclusion. $\rho_s$ and $\rho_f$ are the mass densities of the solid grains and the pore fluid, respectively, and $\rho_{\text{a}} = (1 - \phi)\rho_s + \phi\rho_f$ is the mass density of the composite. $\kappa = k/\eta_f$ denotes the fluid mobility, where $k$ is the absolute permeality and $\eta_f$ is the fluid viscosity. The factor $C_1$ depends on the geometry of the pores: $C_1$ is related the tortuosity of the fluid path, $a_t$, by the equation, $C_1 = 1 - a_t$ (Schanz, 2009). Various approximations for $C_1$ can be found in the literature (Schanz, 2009; Bourbié et al., 1987). Here, we use $C_1 = \frac{1}{2}(1 - \frac{1}{\phi})$. In Eqs. (21a), (21b), $\alpha$ is Biot's effective stress coefficient. Various correlations between the effective stress coefficient ($\alpha$) and the porosity of the poroelastic solid ($\phi$) are available in the literature (Luo et al., 2015; Lee, 2002). In this work, we use $\alpha = 1-(1-\phi)^{3.8}$. The boundary between the poroelastic and the elastic region is denoted by $\Gamma_a$ (Fig. 2). We enforce the following interface conditions on $\Gamma_a$:

$$\mathbf{w} \cdot \mathbf{n}_a^- = 0, \mathbf{x} \in \Gamma_a, \tag{23a}$$

$$\mathbf{u}_a = \mathbf{u}_b, \mathbf{x} \in \Gamma_a, \tag{23b}$$

$$\sigma_a^T \mathbf{n}_a^- = -\sigma_b^T \mathbf{n}_a^+, \mathbf{x} \in \Gamma_a; \quad \text{where,} \tag{23c}$$

$$\sigma_a = \mu_a (\nabla \mathbf{u}_a + \nabla \mathbf{u}_a^T) + \{(\lambda_a + \alpha^2 M) \operatorname{div} \mathbf{u}_a + \alpha M \operatorname{div} \mathbf{w}\} \mathbf{I}, \tag{23d}$$

$$\sigma_b = \mu_b (\nabla \mathbf{u}_b + \nabla \mathbf{u}_b^T) + \{\lambda_b \operatorname{div} \mathbf{u}_b\} \mathbf{I}. \tag{23e}$$

The first interface condition (Eq. (23a)) ensures that the fluid does not flow from the poroelastic inclusion into the elastic host, whereas the second interface condition (Eq. (23b)) enforces the continuity of the solid displacement between the elastic host and the poroelastic inclusion. The final interface condition (Eq. (23c)) implies the continuity of traction on $\Gamma_a$. We assume silent initial conditions for the pore fluid, i.e.,

$$\mathbf{w}(\mathbf{x}, 0) = \dot{\mathbf{w}}(\mathbf{x}, 0) = 0. \tag{24}$$

The governing equations in the heterogeneous elastic host ($\Omega_{reg}$, Fig. 2) and the PML region ($\Omega_{PML}$, Fig. 2) remain same as before (Eqs. (2a), (2b), (2c)) – the response in $\Omega_{reg}$ (Fig. 2) is described by the $\mathbf{u}_b$ displacement field, and that in the PML region ($\Omega_{PML}$) is described by a displacement field ($\mathbf{u}_b$) and a stress history field ($\mathbf{S}$). The initial boundary value problem (IBVP) for wave propagation in the composite (elastic-poroelastic) domain is given by governing partial differential Eqs. (21a), (21b), (2); boundary conditions (4); interface conditions (5), (23); and initial conditions (6), (24). We resolve the IBVP using the finite element method. The details of the finite element formulation can be found in (Karve and Kallivokas, 2015). Thus, given the material and geometric description of the geostructure in question and the definition of the applied forces, we can compute the solid and fluid displacement (velocity and acceleration) field in the poroelastic inclusion by solving the spatio-temporally descretized forward problem, which is similar to the one given by Eq. (12). We remark that the global mass, damping and stiffness matrices for the composite domain are different than those for the elastic domain, and that the vector of unknowns (y) now contains the nodal seepage displacements, as well, i.e.,

$$\mathbf{y} = \left[\tilde{\mathbf{w}}_1\, \tilde{\mathbf{w}}_2\, \tilde{\mathbf{u}}_{a_1}\, \tilde{\mathbf{u}}_{a_2} \middle| \tilde{\mathbf{u}}_{b_1}^{reg}\, \tilde{\mathbf{u}}_{b_2}^{reg} \middle| \tilde{\mathbf{u}}_{b_1}^{PML}\, \tilde{\mathbf{u}}_{b_2}^{PML}\, \tilde{\mathbf{S}}_{11}\, \tilde{\mathbf{S}}_{22}\, \tilde{\mathbf{S}}_{12}\right]^T. \tag{25}$$

Next, we illustrate the uncertainty quantification procedure for the poroelastodynamic system. We use a synthetically created geological formation model, whose geometrical properties are given in Fig. 5a.

**Table 5**
Material properties for the elastic layers in the composite elastic-poroelastic geological formation model (Fig. 5(a)).

| Layer | $\lambda_{b_i}$ (MPa) | $\mu_{b_i}$ (MPa) | $\rho$ kg/$m^3$ |
|---|---|---|---|
| L1 | 416.67 | 625.00 | 1800 |
| L2 | 694.44 | 1041.67 | 2000 |
| L3 | 972.22 | 1458.33 | 2200 |
| L4 | 1250.00 | 1875.00 | 2400 |

**Table 6**
Material properties for the poroelastic inclusion (T) in the composite elastic-poroelastic geological formation model (Fig. 5(a)).

| $\lambda_s$ (MPa) | $\mu_s$ (MPa) | $\lambda_f$ (MPa) | $\rho_s$ (kg/$m^3$) | $\rho_f$ (kg/$m^3$) | $\phi$ | $\kappa = k/\eta_f$ (Darcy m s/kg) |
|---|---|---|---|---|---|---|
| 555.56 | 833.33 | 2000.00 | 2200 | 860 | 0.25 | 100 |

The material properties of the heterogeneous elastic host and the poroelastic inclusion are given in Tables 5 and 6.

We excite the composite solid using three horizontally polarized surface loads whose spatial description is given by Eq. (8), and whose center lines are located at $\eta_1 = -7.00\text{m}, \eta_2 = -5.00\text{m}, \eta_3 = 0.00\text{m}$. Temporally, we use $f_i(t) = (50\text{kN/m}^2)\sin[2\pi(52)t], i = 1, 2, 3$ (load case C). Our goal is to perform sensitivity and uncertainty analysis to quantify the uncertainty in energy delivery to the pore fluid due to the uncertainty in the material parameters. Here, we define a motion metric in terms of the time-averaged kinetic energy of the fluid particles to measure wave energy delivery:

$$\mathrm{KE}_{inc}^{f} = \int_{\Omega_a} \int_0^T \frac{1}{2} \rho_f [\dot{\mathbf{u}}_f(t) \cdot \dot{\mathbf{u}}_f(t)] dt\, d\Omega / T = \int_0^T \frac{1}{2} \dot{\tilde{\mathbf{u}}}_f(t)^T \mathbf{M}_{inc}^f \dot{\tilde{\mathbf{u}}}_f(t) dt / T. \tag{26}$$

Furthermore, we choose the Lamé parameters for the elastic ($\lambda_{b_1}, \ldots, \lambda_{b_4}, \mu_{b_1}, \ldots, \mu_{b_4}$) and poroelastic ($\lambda_s, \mu_s$) solids, as well as the first Lamé parameter for the pore fluid ($\lambda_f$) as the system parameters. We assume that the values of other material constants are known with confidence. Thus, for the case of composite solid (Fig. 5(a)),

$$\mathbf{q} = [q_1\, q_2 \ldots q_N]^T = \left[\lambda_{b_1}\, \lambda_{b_2} \ldots \lambda_s\, \lambda_f\, \mu_{b_1}\, \mu_{b_2} \ldots \mu_s\right]^T. \tag{27}$$

Next, we perform the sensitivity analysis outlined in Section 4 to compute the derivatives of the motion metric with respect to the system parameters. The results are given in Table 7. Once again, we observe that the fluid motion is more sensitive to the value of the second Lamé parameters for the second layer (L2) and for the target inclusion (T).

**Table 7**
Results of sensitivity analysis for the composite solid (load case C).

| $q_i$ | $\frac{\partial \mathrm{KE}_{inc}^f}{\partial q_i}$ (nJ/mPa) | $q_i$ | $\frac{\partial \mathrm{KE}_{inc}^f}{\partial q_i}$ (nJ/mPa) |
|---|---|---|---|
| $\lambda_{b_1}$ | 0.3520 | $\mu_{b_1}$ | 0.5716 |
| $\lambda_{b_2}$ | 0.0413 | $\mu_{b_2}$ | −0.7597 |
| $\lambda_{b_3}$ | −0.0007 | $\mu_{b_3}$ | −0.2572 |
| $\lambda_{b_4}$ | 0.0033 | $\mu_{b_4}$ | 0.1432 |
| $\lambda_s$ | −0.0267 | $\mu_s$ | −0.7103 |
| $\lambda_f$ | −0.0032 | - | - |

**Table 8**
$C_v$ values for different material parameters (scenario 2 in Fig. 9).

| $q_i$ | $C_v$ | $q_i$ | $C_v$ |
|---|---|---|---|
| $\lambda_{b_1}$ | 0.05 | $\mu_{b_1}$ | 0.05 |
| $\lambda_{b_2}$ | 0.10 | $\mu_{b_2}$ | 0.10 |
| $\lambda_{b_3}$ | 0.15 | $\mu_{b_3}$ | 0.15 |
| $\lambda_{b_4}$ | 0.20 | $\mu_{b_4}$ | 0.20 |
| $\lambda_s$ | 0.17 | $\mu_s$ | 0.17 |
| $\lambda_f$ | 0.17 | - | - |

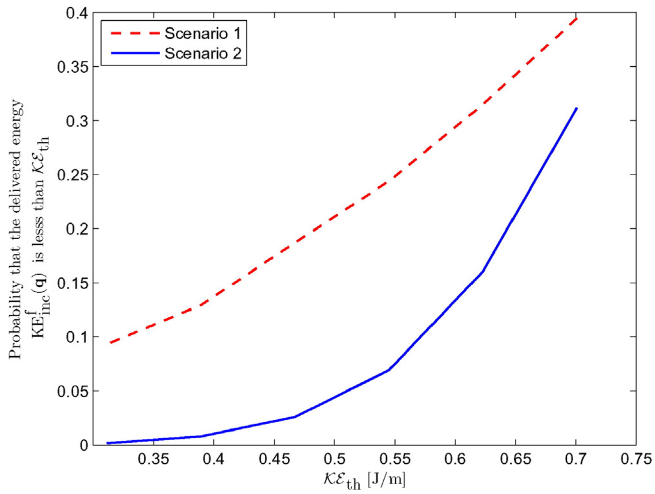


**Fig. 9.** Results of uncertainty analyses for the composite (elastic-poroelastic) geological formation model (load case C), scenario 1: uncertainty analysis using $C_v = 0.2$ for all system variables, scenario 2: uncertainty analysis using the $C_v$ values given in Table 8.

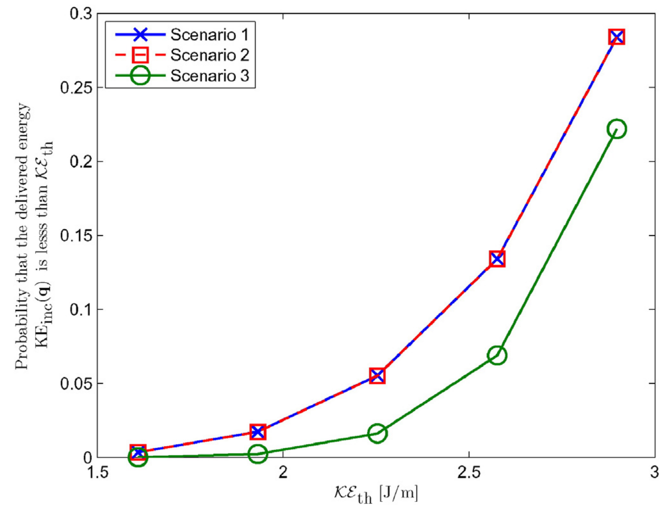


**Fig. 10.** The effect of treating system parameters as deterministic variables, scenario 1: uncertainty analysis treating all Lamé parameters as random variables, scenario 2: uncertainty analysis when the first Lamé parameters for all layers are treated as deterministic variables, and scenario 3: uncertainty analysis when the second Lamé parameter for the first layer ($\mu_{b_1}$) is treated as a deterministic variable.

Lastly, we study the motion metric probabilistically by assuming that the material properties are uncorrelated random variables described by standard normal PDFs. We assume that the Lamé parameter values given in Tables 5 and 6 are the mean values. We compute probabilities of failure to attain threshold values of the motion metric ($KE^{f}_{inc}$) for different $C_v$ values. The results are plotted in Fig. 9. It can be observed in Fig. 9 that $P[KE_{inc}(\mathbf{q}) < \mathcal{KE}_{th}]$ reduces with the value of $\mathcal{KE}_{th}$ for given values of $C_v$. Furthermore, we observe that for a given value of kinetic energy ($\mathcal{KE}_{th}$), $P[KE_{inc}(\mathbf{q}) < \mathcal{KE}_{th}]$ increases as the values of $C_v$ increase.

## 7. Discussion

In this work, we outlined a systematic framework to assess the reliability of wave energy delivery to subsurface formations. We demonstrated the uncertainty quantification procedure using a synthetically created, layered geo-formation (Fig. 5(a)). We remark that the methodology is independent of the optimality of the source characteristics, the spatial dimensionality of the problem (as long as the governing equations remain second-order in time), the type of probability distributions used to model the uncertainty, and the degree of correlation between the system variables.

The results of the first-order uncertainty analysis can be used to estimate the relative error in the probability of failure to attain the threshold $\mathcal{KE}_{th}$, when a material property is treated as a deterministic variable (Madsen, 1988). As an illustration, we consider the uncertainty analysis for load case A and $C_v = 0.2$ (for all layers), and treat some of the system parameters as deterministic variables at their mean values. The results are plotted in Fig. 10. It can be seen in Fig. 10 that the uncertainty analysis results show very small changes when the first Lamé parameters ($\lambda_{b1}, \ldots \lambda_{b4}, \lambda_a$) are treated as deterministic variables (compare scenarios 1 and 2). On the other hand, treating the second Lamé parameter for the first layer ($\mu_{b1}$) as a deterministic variable changes the probability by about 20%-90% (compare scenarios 1 and 3). Thus, neglecting the first Lamé parameters from the uncertainty analysis has a negligible effect on the results, and hence, the computational cost of the uncertainty analysis can be reduced by lowering the parameter space dimension from $N$ to $N/2$.

The assumption about accurate knowledge of the interface geometries can be relaxed by parameterizing interface geometries and treating the geometric parameters as random variables. The deterministic wave physics simulations can be performed for the mean, or expected, interface geometries. The sensitivity of the motion metric to the value of each geometric parameter (and hence, a particular geometry of the interface) can be calculated numerically. Once the derivatives of the motion metric with respect to interface parameters are computed, the uncertainty analysis can be performed in the manner similar to the one presented here.

Next, we discuss a design procedure for the field implementation of the wave-based enhanced oil recovery (EOR) method, as an example. In general, the engineering design of wave-based EOR may involve deciding the following: a) the number of wave sources, b) the capabilities of wave sources (maximum amplitude, frequency range, etc.), c) the duration for which the stress wave stimulation is applied, d) the type of the sources (down-hole or surface sources), and e) the frequency content and locations of the sources. These characteristics can be designed using the following steps:

1. Choose the number, type(s), and maximum amplitude of the wave sources.
2. Obtain or estimate the mean values of the material properties of the layers (and, possibly, the interface geometries) as well as the corresponding variances for the layered geostructure of interest.
3. Define a suitable motion metric of the target layer to assess the intensity of wave energy focusing and the efficiency of trapped (oil) particle removal.
4. Compute the optimal (or, advantageous) source characteristics using: a) a simulation-based method (frequency sweep, inverse-source, or, TR), and b) the mean values of material properties and interface geometries.
5. Perform the uncertainty analysis to compute the probabilities of failure to achieve threshold values of the motion metric.
6. Use the results of the uncertainty analysis and pore-scale dynamics studies to decide the economic and engineering feasibility of the EOR process.
7. If required, change the number, type(s), maximum amplitude of sources, etc., and repeat steps 1 through 6

We remark that a similar approach can be used for contaminant removal or applications where wave energy focusing to geological formations is of importance, and/or the scheduling and optimizing of hydraulic fracturing operations.

## 8. Conclusions

The methodology discussed in this article provides a systematic framework for quantifying the reliability of wave energy delivery to subsurface formations. The results of our uncertainty analysis show that the spatio-temporally optimal sources have a better chance of delivering stress wave stimulation to the targeted geological formation than temporally optimal sources. The procedure discussed in this article can be used to implement the wave-based enhanced oil recovery method in the field.


## Acknowledgments

The first two authors were partially supported by an Academic Excellence Alliance grant between the King Abdullah University of Science and Technology in Saudi Arabia (KAUST) and the University of Texas at Austin. This support is gratefully acknowledged.


## Appendix A. Derivatives of element matrices (elastic target inclusion)

Here, we provide concise definitions of derivatives of element matrices that form the global matrices in Eq. (17). We differentiate the constituents of element matrices given in (Karve et al., 2015; Kucukcoban and Kallivokas, 2013) with respect to Lamé parameters ($\lambda$ or $\mu$). The relevant derivatives are given below:

$$\begin{aligned}\frac{\partial \mathbf{N}_{ik}}{\partial \lambda_b} &= \int_{\Omega_{PML}} k\frac{-1}{4(\mu_b+\lambda_b)^2}\boldsymbol{\Psi}\boldsymbol{\Psi}^T d\Omega, \quad \text{if } i=1,\\ &= \int_{\Omega_{PML}} k\frac{1}{4(\mu_b+\lambda_b)^2}\boldsymbol{\Psi}\boldsymbol{\Psi}^T d\Omega, \quad \text{if } i=2,\\ &= 0, \quad \text{if } i=3,\end{aligned}$$

$$\begin{aligned}\frac{\partial \mathbf{N}_{ik}}{\partial \mu_b} &= \int_{\Omega_{PML}} k\frac{-2\mu_b^2-\lambda_b^2-2\lambda_b\mu_b}{4(\mu_b^2+\lambda_b\mu_b)^2}\boldsymbol{\Psi}\boldsymbol{\Psi}^T d\Omega, \quad \text{if } i=1,\\ &= \int_{\Omega_{PML}} k\frac{-2\mu_b\lambda_b-\lambda_b^2}{4(\mu_b^2+\lambda_b\mu_b)^2}\boldsymbol{\Psi}\boldsymbol{\Psi}^T d\Omega, \quad \text{if } i=2,\\ &= \int_{\Omega_{PML}} k\frac{-1}{\mu_b^2}\boldsymbol{\Psi}\boldsymbol{\Psi}^T d\Omega, \quad \text{if } i=3,\end{aligned}$$

where $\boldsymbol{\Psi}$ are the shape functions used to approximate the stress history variables in the PML region.

For a finite element within the elastic target inclusion, the derivatives of element mass, damping, and stiffness matrices are given by:

$$\begin{aligned}&\frac{\partial \mathbf{M}_a}{\partial \lambda_a} = \frac{\partial \mathbf{M}_a}{\partial \mu_a} = 0, \quad \frac{\partial \mathbf{C}_a}{\partial \lambda_a} = \frac{\partial \mathbf{C}_a}{\partial \mu_a} = 0,\\ &\frac{\partial \mathbf{K}_a}{\partial \lambda_a} = \begin{bmatrix}\mathbf{Q}_{11}^a & \mathbf{Q}_{12}^a\\ \mathbf{Q}_{21}^a & \mathbf{Q}_{22}^a\end{bmatrix},\\ &\frac{\partial \mathbf{K}_a}{\partial \mu_a} = \begin{bmatrix}2\mathbf{Q}_{11}^a+\mathbf{Q}_{22}^a & \mathbf{Q}_{21}^a\\ \mathbf{Q}_{12}^a & 2\mathbf{Q}_{22}^a+\mathbf{Q}_{11}^a\end{bmatrix}.\end{aligned}$$

Derivatives of the element matrices for the regular domain are:

$$\begin{aligned}&\frac{\partial \mathbf{M}_{reg}}{\partial \lambda_b} = \frac{\partial \mathbf{M}_{reg}}{\partial \mu_b} = 0, \quad \frac{\partial \mathbf{C}_{reg}}{\partial \lambda_b} = \frac{\partial \mathbf{C}_{reg}}{\partial \mu_b} = 0,\\ &\frac{\partial \mathbf{K}_{reg}}{\partial \lambda_b} = \begin{bmatrix}\mathbf{Q}_{11}^{reg} & \mathbf{Q}_{12}^{reg}\\ \mathbf{Q}_{21}^{reg} & \mathbf{Q}_{22}^{reg}\end{bmatrix},\\ &\frac{\partial \mathbf{K}_{reg}}{\partial \mu_b} = \begin{bmatrix}2\mathbf{Q}_{11}^{reg}+\mathbf{Q}_{22}^{reg} & \mathbf{Q}_{12}^{reg}\\ \mathbf{Q}_{21}^{reg} & 2\mathbf{Q}_{22}^{reg}+\mathbf{Q}_{11}^{reg}\end{bmatrix}.\end{aligned}$$

In the PML region, derivatives of the element matrices can be computed as:

$$\frac{\partial \mathbf{M}_{PML}}{\partial \gamma} = \begin{bmatrix}0&0&0&0&0\\0&0&0&0&0\\0&0&\frac{-\partial \mathbf{N}_{1a}}{\partial\gamma}&\frac{\partial \mathbf{N}_{2a}}{\partial\gamma}&0\\0&0&\frac{\partial \mathbf{N}_{2a}}{\partial\gamma}&\frac{-\partial \mathbf{N}_{1a}}{\partial\gamma}&0\\0&0&0&0&\frac{-\partial \mathbf{N}_{3a}}{\partial\gamma}\end{bmatrix},$$

$$\frac{\partial \mathbf{C}_{PML}}{\partial \gamma} = \begin{bmatrix}0&0&0&0&0\\0&0&0&0&0\\0&0&\frac{-\partial \mathbf{N}_{1b}}{\partial\gamma}&\frac{\partial \mathbf{N}_{2b}}{\partial\gamma}&0\\0&0&\frac{\partial \mathbf{N}_{2b}}{\partial\gamma}&\frac{-\partial \mathbf{N}_{1b}}{\partial\gamma}&0\\0&0&0&0&\frac{-\partial \mathbf{N}_{3b}}{\partial\gamma}\end{bmatrix},$$

$$\frac{\partial \mathbf{K}_{PML}}{\partial \gamma} = \begin{bmatrix}0&0&0&0&0\\0&0&0&0&0\\0&0&\frac{-\partial \mathbf{N}_{1c}}{\partial\gamma}&\frac{\partial \mathbf{N}_{2c}}{\partial\gamma}&0\\0&0&\frac{\partial \mathbf{N}_{2c}}{\partial\gamma}&\frac{-\partial \mathbf{N}_{1c}}{\partial\gamma}&0\\0&0&0&0&\frac{-\partial \mathbf{N}_{3c}}{\partial\gamma}\end{bmatrix},$$

where $\gamma = \lambda_b$ or $\mu_b$.

## Appendix B. Derivatives of element matrices (poroelastic target inclusion)

Here, we provide concise definitions of derivatives of element matrices that form the global matrices for the composite (elastic-poroelastic) domain. We differentiate the constituents of element matrices given in (Karve and Kallivokas, 2015) with respect to Lamé parameters ($\lambda_s$, $\lambda_f$, or $\mu_s$). For a finite element within the poroelastic target inclusion, the derivatives of element mass and damping matrices are given by:

$$\frac{\partial \mathbf{M}_a}{\partial \lambda_s} = \frac{\partial \mathbf{M}_a}{\partial \mu_s} = \frac{\partial \mathbf{M}_a}{\partial \lambda_f} = 0, \quad \frac{\partial \mathbf{C}_a}{\partial \lambda_s} = \frac{\partial \mathbf{C}_a}{\partial \mu_s} = \frac{\partial \mathbf{C}_a}{\partial \lambda_f} = 0. \tag{B.1}$$

The element stiffness matrix can be written as:

$$\mathbf{K}_a = \begin{bmatrix} M\mathbf{Q}_{11,ww}^a & M\mathbf{Q}_{12,ww}^a & \alpha M\mathbf{Q}_{11,wu}^a & \alpha M\mathbf{Q}_{12,wu}^a\\ M\mathbf{Q}_{21,ww}^a & M\mathbf{Q}_{22,ww}^a & \alpha M\mathbf{Q}_{21,wu}^a & \alpha M\mathbf{Q}_{22,wu}^a\\ \alpha M\mathbf{Q}_{11,uw}^a & \alpha M\mathbf{Q}_{12,uw}^a & (2\mu_s+D_1)\mathbf{Q}_{11,uu}^a+\mu_s\mathbf{Q}_{22,uu}^a & \mu_s\mathbf{Q}_{21,uu}^a+D_1\mathbf{Q}_{12,uu}^a\\ \alpha M\mathbf{Q}_{21,uw}^a & \alpha M\mathbf{Q}_{22,uw}^a & \mu_s\mathbf{Q}_{12,uu}^a+D_1\mathbf{Q}_{21,uu}^a & (2\mu_s+D_1)\mathbf{Q}_{22,uu}^a+\mu_s\mathbf{Q}_{11,uu}^a\end{bmatrix}, \tag{B.2}$$

where $D_1 = \lambda_a + \alpha^2 M$, and $\mathbf{Q}_{ij,pq}^a$ are defined in (Karve and Kallivokas, 2015). The derivatives of the element stiffness matrix can be calculated using,

$$\frac{\partial \lambda_a}{\partial \lambda_s} = 1-\alpha, \tag{B.3}$$

$$\frac{\partial \lambda_a}{\partial \mu_s} = -\frac{2}{3}\alpha, \tag{B.4}$$

$$\frac{\partial \lambda_a}{\partial \lambda_f} = 0, \tag{B.5}$$

$$\frac{\partial M}{\partial \lambda_s} = \frac{\lambda_f}{D} - \frac{\phi\lambda_f\left(\lambda_s+\frac{2}{3}\mu_s\right)}{D^2}, \tag{B.6}$$

$$\frac{\partial M}{\partial \mu_s} = \frac{\frac{2}{3}\lambda_f}{D} - \frac{\frac{2}{3}\phi\lambda_f\left(\lambda_s + \frac{2}{3}\mu_s\right)}{D^2}, \tag{B.7}$$

$$\frac{\partial M}{\partial \lambda_f} = \frac{\lambda_s + \frac{2}{3}\mu_s}{D} - \frac{(\alpha-\phi)\lambda_f\left(\lambda_s + \frac{2}{3}\mu_s\right)}{D^2}, \tag{B.8}$$

where $D = (\alpha-\phi)\lambda_f + \phi(\lambda_s + \frac{2}{3}\mu_s)$. Note that the derivatives of the element matrices for the elastic host and for the PML region remain the same as those given in Appendix A.

## Appendix C. the Rackwitz-Fiessler algorithm

The Rackwitz-Fiessler algorithm for uncorrelated, normally distributed random variables ($q_i$, $i = 1,2,\ldots,N$) is given below.

**Table C.9**
The Rackwitz-Fiessler algorithm.

| | |
|---|---|
| 0 | Choose a candidate load description and the value for the threshold ($\mathcal{KE}_{\text{th}}$) |
| | Define $g(\mathbf{q}) = \text{KE}_{\text{inc}}(\mathbf{q}) - \mathcal{KE}_{\text{th}}$ |
| | $\therefore P[\text{KE}_{\text{inc}}(\mathbf{q}) < \mathcal{KE}_{\text{th}}] = P[g(\mathbf{q}) < 0]$ |
| 1 | Set $k = 0, \mathbf{q}^k = \mathbf{q}^0, \bar{\mathbf{q}}, \mathbf{D}$, and tolerance $tol$ |
| 2 | $U_i^k = (q_i^k - \bar{q}_i)/D_i,\ i = 1, 2 \ldots N.$ |
| 3 | $\beta^k = \sqrt{\sum_{i=1}^{N}(U_i^k)^2}$ |
| 4 | $g(\mathbf{U}^k) = g(\mathbf{q}^k) = g$ , |
| 5 | $(\boldsymbol{\nabla} g)_i = \frac{\partial g}{\partial U_i}\Big\rvert_{\mathbf{U}^k} = \frac{\partial g}{\partial q_i}\Big\rvert_{\mathbf{q}^k} \times D_i = \frac{\partial \text{KE}_{\text{inc}}}{\partial q_i}\Big\rvert_{\mathbf{q}^k} \times D_i$ (equation 19) |
| 6 | $\mathbf{U}^{k+1} = \left\{[(\boldsymbol{\nabla} g)^T\mathbf{U} - g]/\lvert\boldsymbol{\nabla} g\rvert\right\}\boldsymbol{\nabla} g$ |
| 7 | $q_i^{k+1} = U_i^{k+1}D_i + \bar{q}_i$ |
| 8 | IF $k > 1$ AND $\lvert\beta^k - \beta^{k-1}\rvert \le tol$ |
| | $\beta \leftarrow \beta^k$, GO TO STEP 9 |
| | ELSE |
| | $k \leftarrow k+1$, GO TO STEP 3 |
| 9 | $P[\text{KE}_{\text{inc}}(\mathbf{q}) < \mathcal{KE}_{\text{th}}] = P[g(\mathbf{q}) < 0] = \Phi(-\beta)$ |
| | ($\Phi(\cdot)$ is the standard normal cumulative distribution function) |

## References


Anderson, B.E., Griffa, M., Larmat, C., Ulrich, T.J., Johnson, P.A., 2008. Time reversal. Acoust. Today 4 (1), 5–16.

Beresnev, I.A., Deng, W., 2010. Viscosity effects in vibratory mobilization of residual oil. Geophysics 75 (4), N79–N85.

Beresnev, I.A., Johnson, P.A., 1994. Elastic-wave stimulation of oil production: A review of methods and results. Geophysics 59 (6), 1000–1017.

Beresnev, I., Gaul, W., Vigil, R.D., 2011. Direct pore-level observation of permeability increase in two-phase flow by shaking. Geophys. Res. Lett. 38 (20). http://dx.doi.org/10.1029/2011GL048840.

M. A. Biot, Theory of propagation of elastic waves in a fluid saturated porous solid. i. low frequency range, J. Acoust. Soc. Am. 28 (2).

Bourbié, T., Coussy, O., Zinszer, B., 1987. Acoustics of porous media. Gulf publishing company.

Deng, W., Cardenas, M.B., 2013. Dynamics and dislodgment from pore constrictions of a trapped nonwetting droplet stimulated by seismic waves. Water Resour. Res. 49 (7), 4206–4218.

Gouveia, W.P., Scales, J.A., 1998. Bayesian seismic waveform inversion: Parameter estimation and uncertainty analysis. J. Geophys. Res. 103, 2759–2779.

Iassonov, P.P., Beresnev, I.A., 2003. A model for enhanced fluid percolation in porous media by application of low-frequency elastic waves. J. Geophys. Res. Solid Earth 108 (B3). http://dx.doi.org/10.1029/2001JB000683.

Jeong, C., Kallivokas, L., Kucukcoban, S., Deng, W., Fathi, A., 2015. Maximization of wave motion within a hydrocarbon reservoir for wave-based enhanced oil recovery. J. Pet. Sci. Eng. 129 (0), 205–220. http://dx.doi.org/10.1016/j.petrol.2015.03.009.

Karve, P.M., Kallivokas, L.F., 2015. Wave energy focusing to subsurface poroelastic formations to promote oil mobilization. Geophys. J. Int. 202 (1), 119–141. http://dx.doi.org/10.1093/gji/ggv133.

Karve, P.M., Kucukcoban, S., Kallivokas, L.F., 2015. On an inverse source problem for enhanced oil recovery by wave motion maximization in reservoirs. Comput. Geosci. 19 (1), 233–256. http://dx.doi.org/10.1007/s10596-014-9462-7.

Kostrov, S.A., Wooden, B.O., 2002. Mechanisms, field suitability, and case studies for enhancement of oil recovery and production using in-situ seismic stimulation. 16th International Symposium on Nonlinear Acoustics.

Kouznetsov, O., Simkin, E., Chilingar, G., Katz, S., 1998. Improved oil recovery by application of vibro-energy to waterflooded sandstones. J. Pet. Sci. Eng. 19 (3–4), 191–200. http://dx.doi.org/10.1016/S0920-4105(97)00022-3.

Kucukcoban, S., Kallivokas, L., 2013. A symmetric hybrid formulation for transient wave simulations in PML-truncated heterogeneous media. Wave Motion 50 (1), 57–79.

Lee, M.W., 2002. Biot-Gassmann theory for velocities of gas hydrate-bearing sediments. Geophysics 67 (6), 1711–1719.

Lo, W.-C., Sposito, G., Huang, Y.-H., 2012. Modeling seismic stimulation: Enhanced non-aqueous fluid extraction from saturated porous media under pore-pressure pulsing at low frequencies. J. Appl. Geochem. 78, 77–84. http://dx.doi.org/10.1016/j.jappgeo.2011.06.027.

Luo, X., Were, P., Liu, J., Hou, Z., 2015. Estimation of biot's effective stress coefficient from well logs. Environ. Earth Sci. 73 (11), 7019–7028. http://dx.doi.org/10.1007/s12665-015-4219-8.

Madsen, H.O., 1988. Omission sensitivity factors. Struct. Saf. 5 (1), 35–45. http://dx.doi.org/10.1016/0167-4730(88)90004-5.

Manga, M., Beresnev, I., Brodsky, E.E., Elkhoury, J.E., Elsworth, D., Ingebritsen, S.E., Mays, D.C., Wang, C.-Y., 2012. Changes in permeability caused by transient stresses: Field observations, experiments, and mechanisms. Rev. Geophys. 50 (2). http://dx.doi.org/10.1029/2011RG000382.

Pride, S.R., Flekkøy, E.G., Aursjø, O., 2008. Seismic stimulation for enhanced oil recovery. Geophysics 73 (5), O23–O35.

Rackwitz, R., Fiessler, B., 1978. Structural reliability under combined random load sequences. Comput. Struct. 9 (5), 489–494.

Roberts, P.M., Abdel-Fattah, A.I., 2009. Seismic stress stimulation mobilizes colloids trapped in a porous rock. Earth Planet. Sci. Lett. 284 (3), 538–543.

Roberts, P.M., Sharma, A., Uddameri, V., Monagle, M., Dale, D.E., Steck, L.K., 2001. Enhanced DNAPL transport in a sand core during dynamic stress stimulation. Environ. Eng. Sci. 18 (2), 67–79.

Schanz, M., 2009. Poroelastodynamics: Linear Models, Analytical Solutions, and Numerical Methods. Appl. Mech. Rev. 62 (3).

Tsikas, A., 1997. Sensitivity analysis of elastodynamic systems (Master's thesis) Department of Civil and Environmental Engineering, Carnegie Mellon University.

Ulrich, T., Van Den Abeele, K., Le Bas, P.-Y., Griffa, M., Anderson, B.E., Guyer, R.A., 2009. Three component time reversal: Focusing vector components using a scalar source. J. Appl. Phys. 106 (11), 113504.

Van Keulen, F., Haftka, R., Kim, N., 2005. Review of options for structural design sensitivity analysis. part 1: Linear systems. Comput. Methods Appl. Mech. Eng. 194 (30), 3213–3243.

Vogler, E.T., Chrysikopoulos, C.V., 2002. Experimental investigation of acoustically enhanced solute transport in porous media. Geophys. Res. Lett. 29 (15), 5-1–5-4. http://dx.doi.org/10.1029/2002GL015304.